Data report: Si, Al, Fe, Ca, and K systematics of volcaniclastic sediments from selected cores of Hole U1347A, IODP Expedition 324[1]

Sandra Herrmann[2] and Nicole A. Stroncik[2]

Chapter contents

[1]Herrmann, S., and Stroncik, N.A., 2013. Data report: Si, Al, Fe, Ca, and K systematics of volcaniclastic sediments from selected cores of Hole U1347A, IODP Expedition 324. *In* Sager, W.W., Sano, T., Geldmacher, J., and the Expedition 324 Scientists, *Proc. IODP,* 324: Tokyo (Integrated Ocean Drilling Program Management International, Inc.). doi:10.2204/iodp.proc.324.204.2013
[2]Integrated Ocean Drilling Program, Texas A&M University, 1000 Discovery Drive, College Station TX 77845, USA. Correspondence author: herrmann@iodp.tamu.edu

Abstract

We analyzed the whole-rock Si, Al, Fe, Ca, K, Cl, and Mn content of volcaniclastic sediment cores recovered during Integrated Ocean Drilling Program Expedition 324 in Hole U1347A. Hole U1347A, located at the eastern flank of Tamu Massif, the oldest of the three volcanic edifices forming Shatsky Rise, a large igneous plateau in the western Pacific, was drilled into early Cretaceous sediments and volcanic basement. The analyzed cores represent the mainly volcaniclastic sediments lying on top of the basaltic basement, which starts at roughly 156.7 meters below seafloor. Whole-rock Si, Al, Fe, Ca, K, Cl, and Mn were obtained from a stratigraphic depth interval covering about 60 m using an Avaatech X-ray fluorescence core scanner. Data interpretation has been based on the normalization of individual element count rates to Ca. In the uppermost 110 m depth interval, increases in the Al/Ca, Fe/Ca, Mn/Ca, K/Ca, and Cl/Ca ratios can be observed. Below this depth, no clear element depth correlation is evident and the average element ratios stay relatively constant throughout the remaining depth interval. However, rhythmic patterns can be observed throughout the entire investigated core material, characterized by positive co-variations of Si/Ca, Al/Ca, Fe/Ca, Mn/Ca, K/Ca, and Cl/Ca with variable amplitudes and peak widths. The geochemical downhole trends of increasing Si/Ca, Al/Ca, Fe/Ca, Mn/Ca, K/Ca, and Cl/Ca clearly reflect the changes in the principal lithology from marine limestone with intercalated chert to volcaniclastic sediment. The observed rhythmic patterns of Si/Ca, Al/Ca, Fe/Ca, Mn/Ca, K/Ca, and Cl/Ca correlate with existing variations in the ratio of volcaniclastic material to carbonaceous material.

Introduction

This report provides the results of a geochemical study of seven cores consisting of biogenic and clastic sediments recovered during Integrated Ocean Drilling Program (IODP) Expedition 324 from Hole U1347A situated close to the summit of Tamu Massif (Fig. F1). Tamu Massif is the main edifice forming Shatsky Rise, and thus sampling this volcano was one of the main objectives of this *JOIDES Resolution* expedition (Sager et al., 2009). The main coring targets of Site U1347 were to recover as much as possible of the oldest sediments overlying the igneous basement and the

doi:10.2204/iodp.proc.324.204.2013

Early Cretaceous igneous basement (Sano et al., 2012). The aim of coring the igneous rocks was to determine the basement age and its geochemical and isotopic characteristics to constrain the age progression and duration of volcanism at Shatsky Rise and its magma sources, temperature and depth of melting and crystallization, and degree of partial melting. Studies of the sediment overlying the igneous basement were intended to constrain the sedimentation rates and processes atop the volcanic rise to better understand the eruption and subsidence history of the rise.

In this context we wanted to test if the geochemical characterization of cored volcaniclastic material by means of high-resolution X-ray fluorescence core scans is a useful tool to investigate the depositional history and the formation of volcaniclastic deposits.

Materials and methods

A total of 17.2 m sediment over a stratigraphic interval of ~60 m (Cores 324-U1347A-3R through 10R) was retrieved from Hole U1347A before entering basaltic basement at 157.6 meters below seafloor (mbsf). The recovered material is dominated by volcaniclastic silt and sandstone with varying proportions of biogenic material (radiolarians and foraminifers) and mainly micritic carbonate (see the **"Site U1347"** chapter [Expedition 324 Scientists, 2010]). The sediment recovered from the 80.5–99.8 mbsf depth interval (Cores 3R and 4R) is composed of mildly silicified radiolarian-bearing glauconitic limestone and sandstone with occasional occurrences of chert. Radiolarians are very common throughout the entire depth interval. The sediments derived from the 99.8–149.1 mbsf depth interval (Cores 5R–10R) consist of alternating layers of volcaniclastic sandy siltstone (Fig. **F2,** Thin Sections 324-U1347A-6R-2, 10–11 and 59–62 cm) and silty sandstone (Fig. **F2,** Thin Section 324-U1347A-6R-1, 38–42 cm) with intercalated very fine grained layers occurring throughout the entire cored interval (Fig. **F2,** Thin Section 324-U1347A-6R-2, 81–84 cm) (Fig. **F3**). Both lithologies contain biogenic material (radiolarians and foraminifers) and micritic carbonate in varying amounts. The very fine grained layers are mainly composed of smectite, completely replacing the fresh glass particles, and minor amounts of micritic carbonate. The volcaniclastic silty sandstone is mainly composed of volcanic particles (including altered plagioclase) being to variable amounts replaced by dark brown clay minerals mixed with biogenic material and micritic carbonate. As much as 25% of the material in this silty sandstone is of nonvolcanic origin. Black oxides (probably Mn oxide) can be found on particle rims. The volcaniclastic sandy siltstone is also composed of the same components as the volcaniclastic silty sandstone. However, the amount of biogenic material and micritic carbonate is much higher than in the volcaniclastic silty sandstone (up to 60%). Radiolarians are common throughout the entire interval, even though in some of the coarser intervals the radiolarians are replaced by secondary calcite.

The material described above has been analyzed between 80.59 mbsf and 149.13 mbsf (68.54 m) for the Si, Al, Fe, Ca, K, Cl, and Mn contents using a third-generation Avaatech X-ray fluorescence (XRF) scanner with a Canberra X-PIPS silicon drift detector (SDD), model SXD 15C-150-500, 150 eV resolution X-ray detector located at the IODP Gulf Coast Repository in College Station, Texas (USA) (**odases.tamu.edu/index.php/research-facilities/**). The X-ray tube and detector are mounted on a moving track so that multiple spots at different depths can be analyzed on a split core during the scanning run. Multiple scans with different settings can be automatically programmed (Richter et al., 2006). Precision of the measurement positioning is 0.1 mm. For Hole U1347A core scans, the sample spacing along each core section was set at 1 cm intervals. The scans were performed at 10 kV using an Al filter. The voltage used for elements measured is determined by the energy needed to excite the appropriate characteristic X-rays. While measuring, the detector registers the emission line energies of the irradiated sample material and their frequency over the predefined measure time (30 s) as element intensities in counts, which are proportional to the element concentrations. The scan was run down the center of the split core half (6.8 cm total diameter). The tube current was set to 2 mA; the dead time of the XRF scanner is between 20% and 40%. Each core section was removed from refrigeration at least 2 h prior to scanning. To protect the detector face from becoming sediment covered and contaminated during the scan, the cores were covered ~15 min before scanning with 4 µm thick Ultralene plastic film (SPEX Centriprep, Inc.).

The processing software used, WinAxil of Canberra, applies background subtraction, sum-peak correction, escapes peak correction, and peak integration of the XRF spectrum. It uses an interactive least-squares fitting procedure of a Gaussian function to approximate the fluorescence lines. The goodness-of-fit of a process model increases if the model identifies all peaks present in the XRF spectrum, as the program does not look at individual peaks but at groups of peaks.

Results and discussion

As XRF count rates for different elements are influenced by different factors, such as sample matrix, surface topography, or porosity, not accounted for in the postprocessing of the data derived from the XRF scanner, direct count rates of individual elements can only be compared with caution. This is especially the case when comparing the count rates of elements that are far apart in the periodic system of elements (e.g., light versus heavy elements). Based on these predefined conditions, the data interpretation in this contribution is entirely based on element ratios. As the cored sediments consist of limestone and volcaniclastic material, which basically represents a three-component mixture of (1) fresh volcanic glass, (2) altered volcanic glass to mainly smectite, and (3) biogenic and micritic carbonate, Si, Al, Fe, Mn, K, and Cl count rates have been normalized to Ca count rates. Because the volcaniclastic material furthermore represents a mixture of fresh and altered glass, Al, Fe, Mn, Ca, K, and Cl count rates have been normalized to the Si count rates. For better visualization of the geochemical patterns, the element ratios displayed in Figure F3 were smoothed by a two-point moving average. Averages of the different ratios for each individual core were calculated (Fig. F4), with the error bars representing the calculated variability (variance) characterizing each core.

Generally, two different systematic patterns in Si/Ca, Al/Ca, Fe/Ca, Mn/Ca, K/Ca, and Cl/Ca were observed in the investigated core material. One trend is a rhythmic pattern of increasing and decreasing element ratios with peak widths being variable throughout the entire core material (Fig. F3). The other one is a consistent downhole pattern of constantly decreasing/increasing element ratios superimposed on these rhythmic patterns (Figs. F3, F4). The latter is most prominent in the uppermost 110 m depth interval and is characterized by a steep increase in the Al/Ca, Fe/Ca, Mn/Ca, K/Ca, and Cl/Ca ratios (Figs. F3, F4). Below this depth, no clear element depth correlation can be observed and the average element ratios stay more or less constant throughout the remaining depth interval. The rhythmic patterns observed throughout the entire investigated core material are characterized by positive co-variations of Si/Ca, Al/Ca, Fe/Ca, Mn/Ca, K/Ca, and Cl/Ca with variable amplitudes and peak widths. Occasionally, the Cl/Ca ratio is anticorrelated to the Al/Ca, Fe/Ca, Mn/Ca, and K/Ca ratios.

The sediment investigated in this study is characterized by two main lithostratigraphic sequences, a sequence of marine limestone with intercalated chert and a roughly 110 m thick volcaniclastic sediment sequence with the limestone being deposited on top of the volcaniclastic material. The geochemical downhole trends of increasing Si/Ca, Al/Ca, Fe/Ca, Mn/Ca, K/Ca, and Cl/Ca clearly reflect this change in the principal lithology (Figs. F3, F4).

The cored volcaniclastic material is characterized, as already described above, by alternating layers of variable grain size, which are consistent with varying mixtures of predominantly altered glass, fresh glass, and biogenic as well as micritic carbonate and occasional intercalated thin layers containing higher abundances of radiolarians (Fig. F3). Geochemically, the mixture of carbonaceous material with the largely altered volcaniclastic material can be visualized as a dilution of the geochemical signal coming solely from the volcanic material. Because one key effect of submarine glass alteration to smectite is the nearly total loss of Ca (e.g., Stroncik and Schmincke, 2002), the observed Si/Ca, Al/Ca, Fe/Ca, Mn/Ca, K/Ca, and Cl/Ca records show the existing variations in the ratio of volcaniclastic material to carbonaceous material. The observed rhythmic patterns of Si/Ca, Al/Ca, Fe/Ca, Mn/Ca, K/Ca, and Cl/Ca correlate with the alternating layers of variable grain sizes observed in the core. An example is the medium grained, homogeneous-looking sediment characterizing the mixture of higher amounts of carbonate with volcanic material that corresponds to lows in the specific element ratios. On the other hand, the fine-grained material, being dominated by altered volcanic glass, corresponds to highs in the specific element ratios (Fig. F3). The higher amount of carbonaceous material, as well as the larger grain size in the medium-sized volcaniclastics, is most likely an indication for a shallower water hyaloclastite emplacement compared to the fine-grained material containing only minor amounts of carbonate.

In Figure F5, Al/Si, Fe/Si, Mn/Si, K/Si, and Cl/Si ratios are plotted versus Si. Even though the data show relatively large scatter, it is evident that Fe/Si, K/Si, and Cl/Si show negative trends with increasing Si content and that Al/Si shows positive trends with Si content in individual cores. This indicates that the geochemical signal introduced by the glass alteration process is superimposed on the "carbonate-volcaniclastic mixing signal" because alteration of basaltic glass to smectite results in a relative enrichment of Fe, K, and Cl and a relative depletion of Si and Al (e.g., Stroncik and Schmincke, 2002).

Conclusions

In this study we have shown that the geochemical characterization of cored volcaniclastic material by

means of high-resolution X-ray fluorescence core scans has the potential to be a useful tool in investigation of the depositional history and the formation of volcaniclastic deposits. In a future study we want to fine-tune this method by conducting additional, detailed thin section studies of the volcaniclastic material cored during IODP Expedition 324 and by obtaining quantitative XRF data from discrete samples of the cored material.

Acknowledgments

We thank IODP for making sample material available to us and David Houpt for letting us use the XRF core scanner. We are thankful for the introduction to the Avaatech XRF core scanner; thank you, Thomas Gorgas. We furthermore want to thank the reviewers of the manuscript for their productive suggestions.

References

Expedition 324 Scientists, 2010. Site U1347. *In* Sager, W.W., Sano, T., Geldmacher, J., and the Expedition 324 Scientists, *Proc. IODP,* 324: Tokyo (Integrated Ocean Drilling Program Management International, Inc.). **doi:10.2204/iodp.proc.324.104.2010**

Richter, T.O., van der Gaast, S., Koster, B., Vaars, A., Gieles, R., de Stigter, H.C., De Haas, H., and van Weering, T.C.E., 2006. The Avaatech XRF Core Scanner: technical description and applications to NE Atlantic sediments. *In* Rothwell, R.G. (Ed.), *New Techniques in Sediment Core Analysis*. Geol. Soc. Spec. Publ., 267(1):39–50. **doi:10.1144/GSL.SP.2006.267.01.03**

Sager, W.W., Sano, T., and Geldmacher, J., 2009. Testing plume and plate models of ocean plateau formation at Shatsky Rise, northwest Pacific Ocean. *IODP Sci. Prosp.,* 324. **doi:10.2204/iodp.sp.324.2009**

Sano, T., Shimizu, K., Ishikawa, A., Senda, R., Chang, Q., Kimura, J.-I., Widdowson, M., and Sager, W.W., 2012. Variety and origin of magmas on Shatsky Rise, northwest Pacific Ocean. *Geochem., Geophys., Geosyst.,* 13(8):Q08010. **doi:10.1029/2012GC004235**

Stroncik, N.A., and Schmincke, H.-U., 2002. Palagonite; a review. *Int. J. Earth Sci.,* 91(4):680–697. **doi:10.1007/s00531-001-0238-7**

Initial receipt: 17 November 2012
Acceptance: 21 May 2013
Publication: 14 October 2013
MS 324-204

Figure F1. Location of Shatsky Rise plateau in relation to Japan (upper right corner). Shaded area illustrates the region of the bathymetric map of the southwest area of the Tamu Massif with the location of Site U1347.

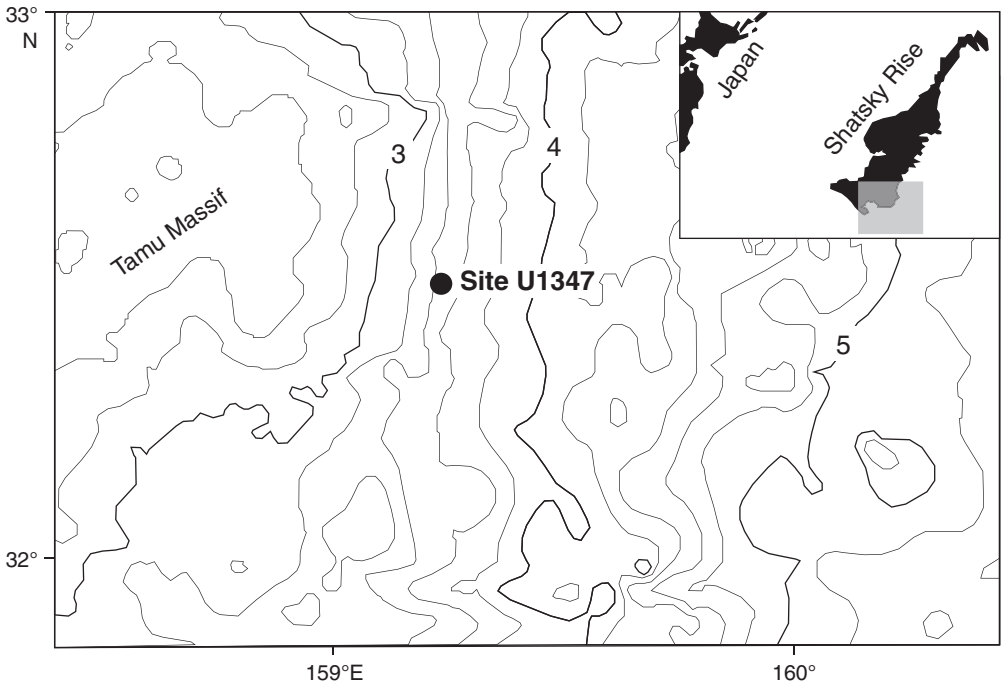

Figure F2. Examples of lithologic intervals based on the thin sections. Scale bar = 2 cm.

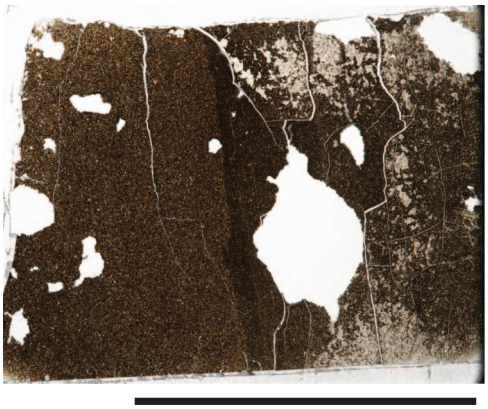

324-U1347A-6R-1, 38-42 cm

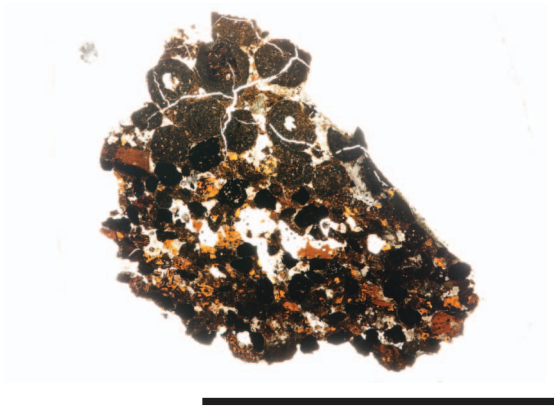

324-U1347A-6R-2, 10-11 cm

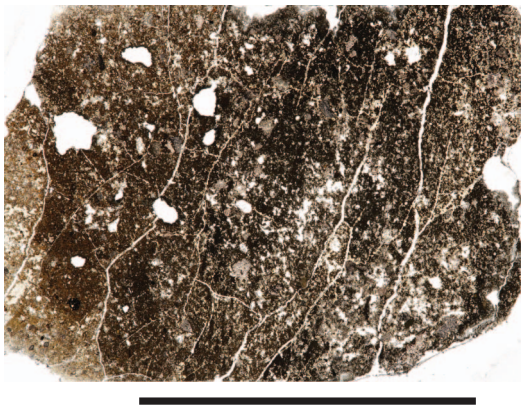

324-U1347A-6R-2, 59-62 cm

324-U1347A-6R-2, 81-84 cm

Figure F3. Recovery from Cores 324-U1347A-3R through 10R and Al/Ca (blue), Fe/Ca (red), Mn/Ca (brown), Si/Ca (dark green), K/Ca (light green), and Cl/Ca (gray) versus depth. (Continued on next six pages.)

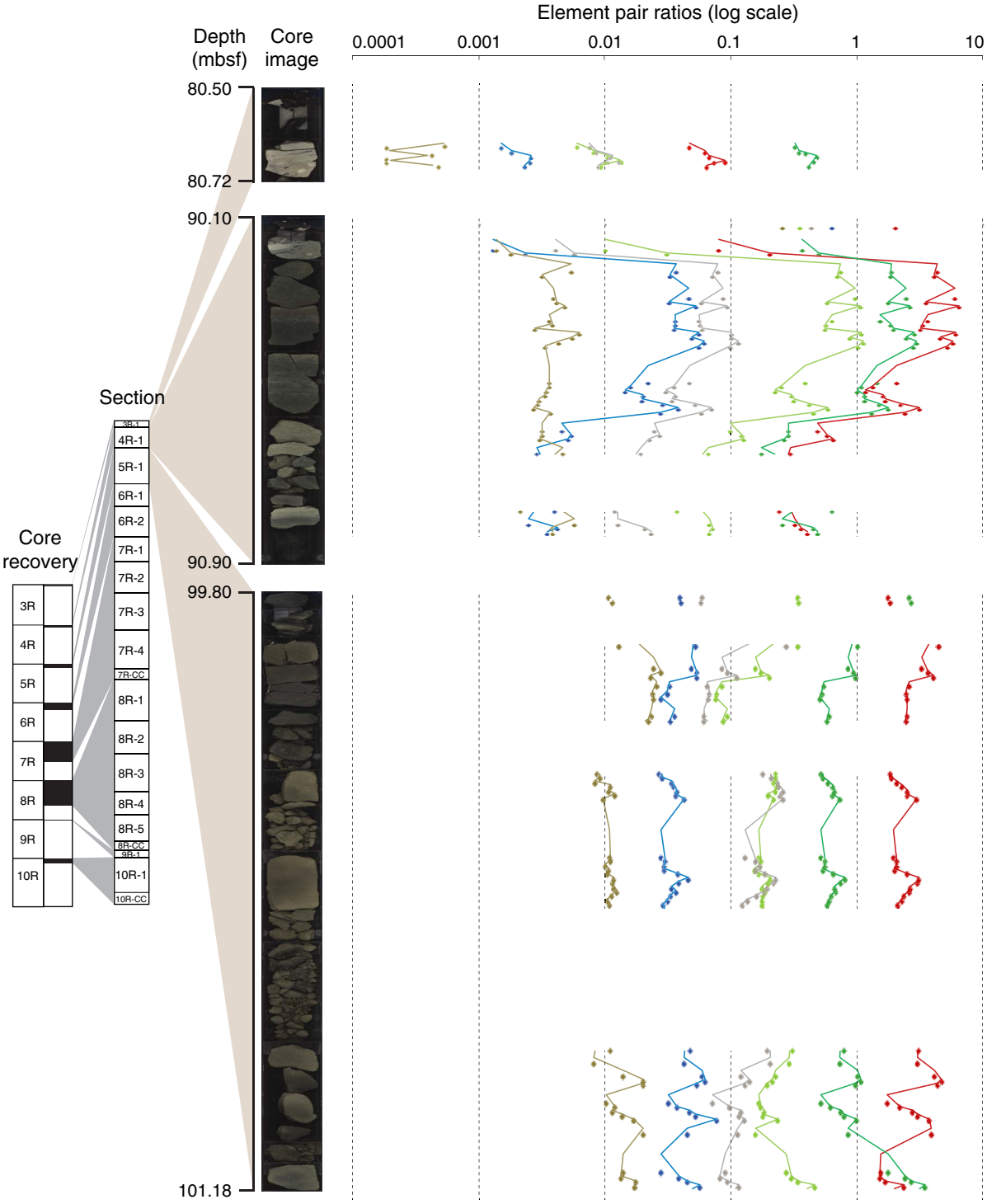

Figure F3 (continued). (Continued on next page.)

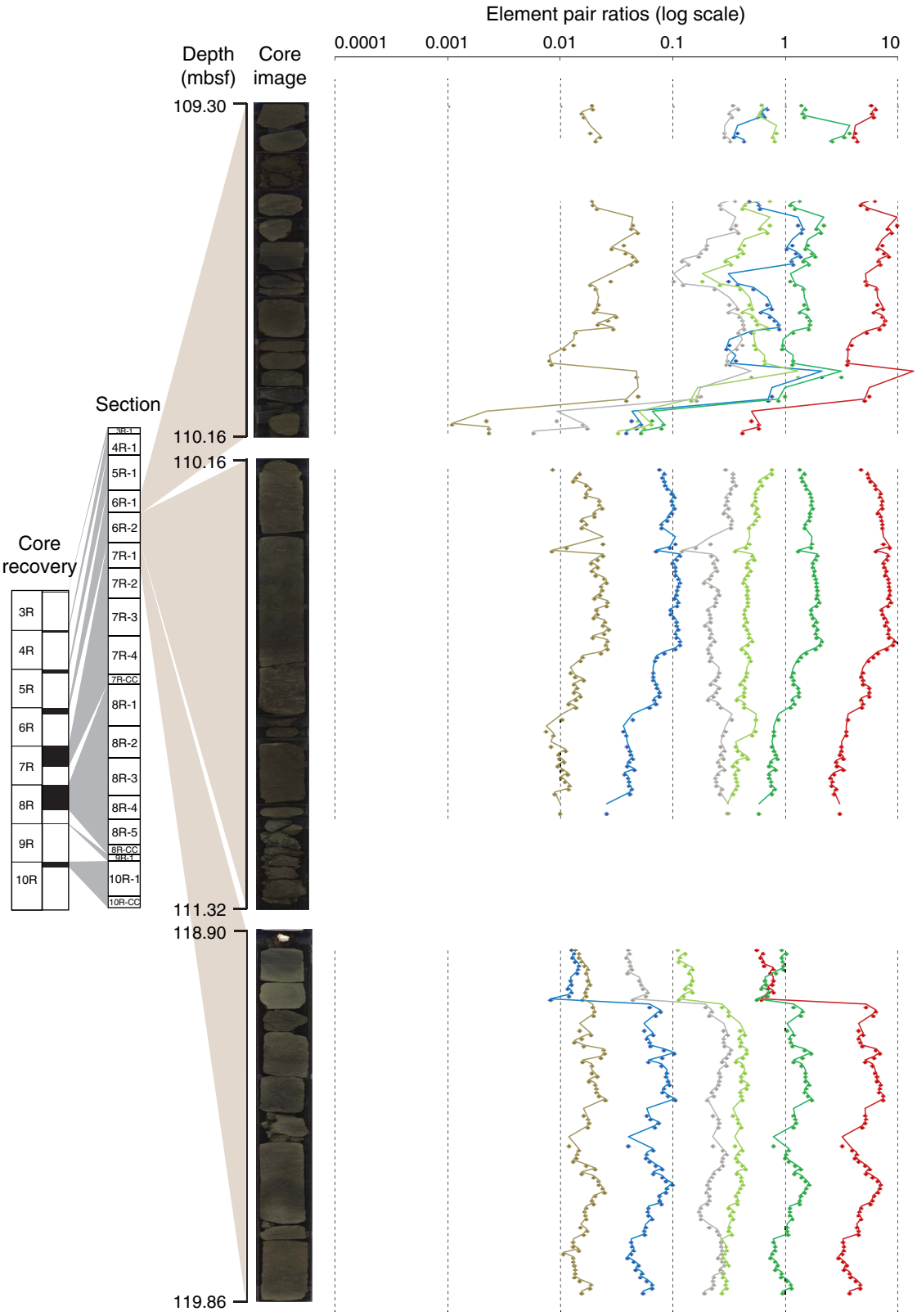

Figure F3 (continued). (Continued on next page.)

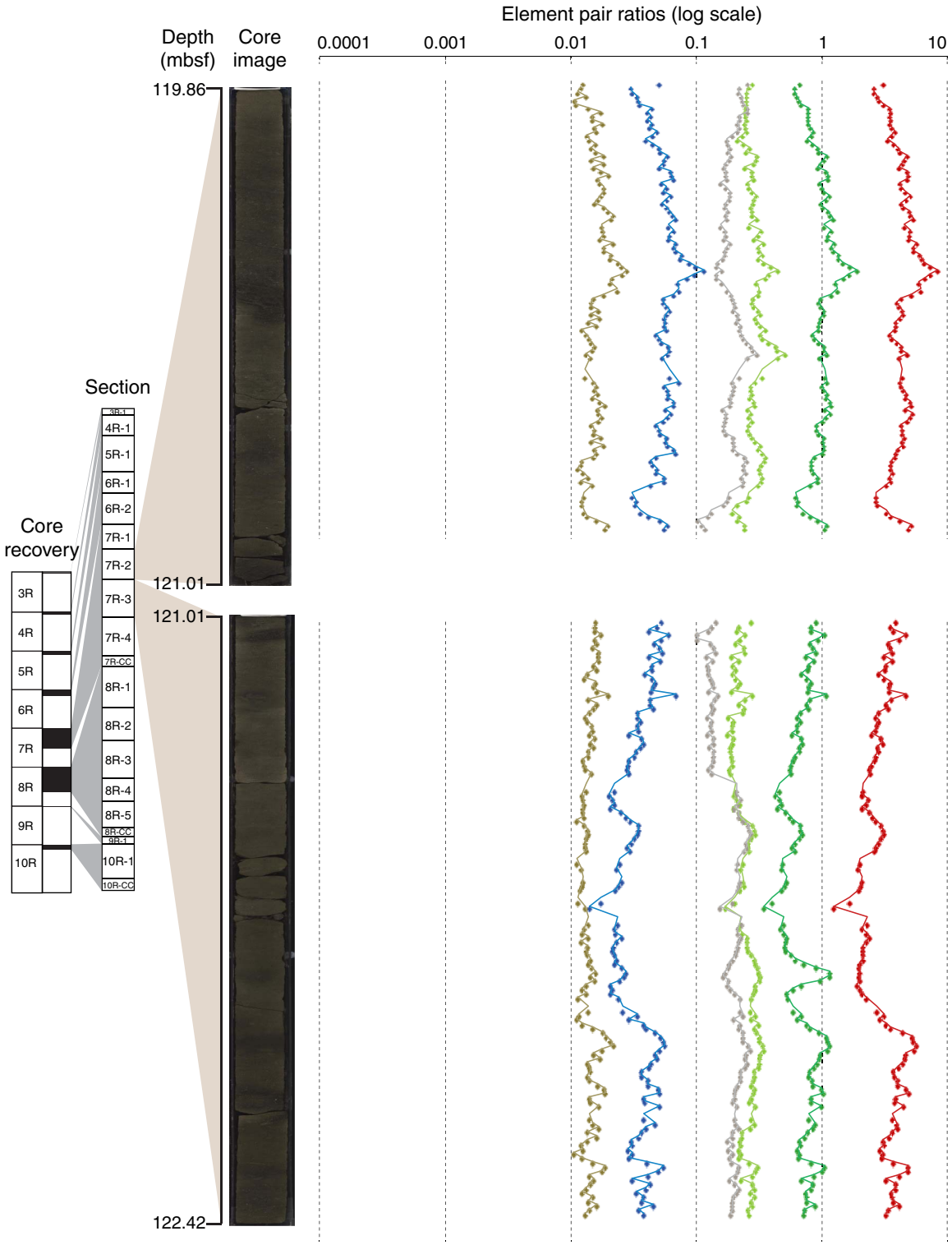

Figure F3 (continued). (Continued on next page.)

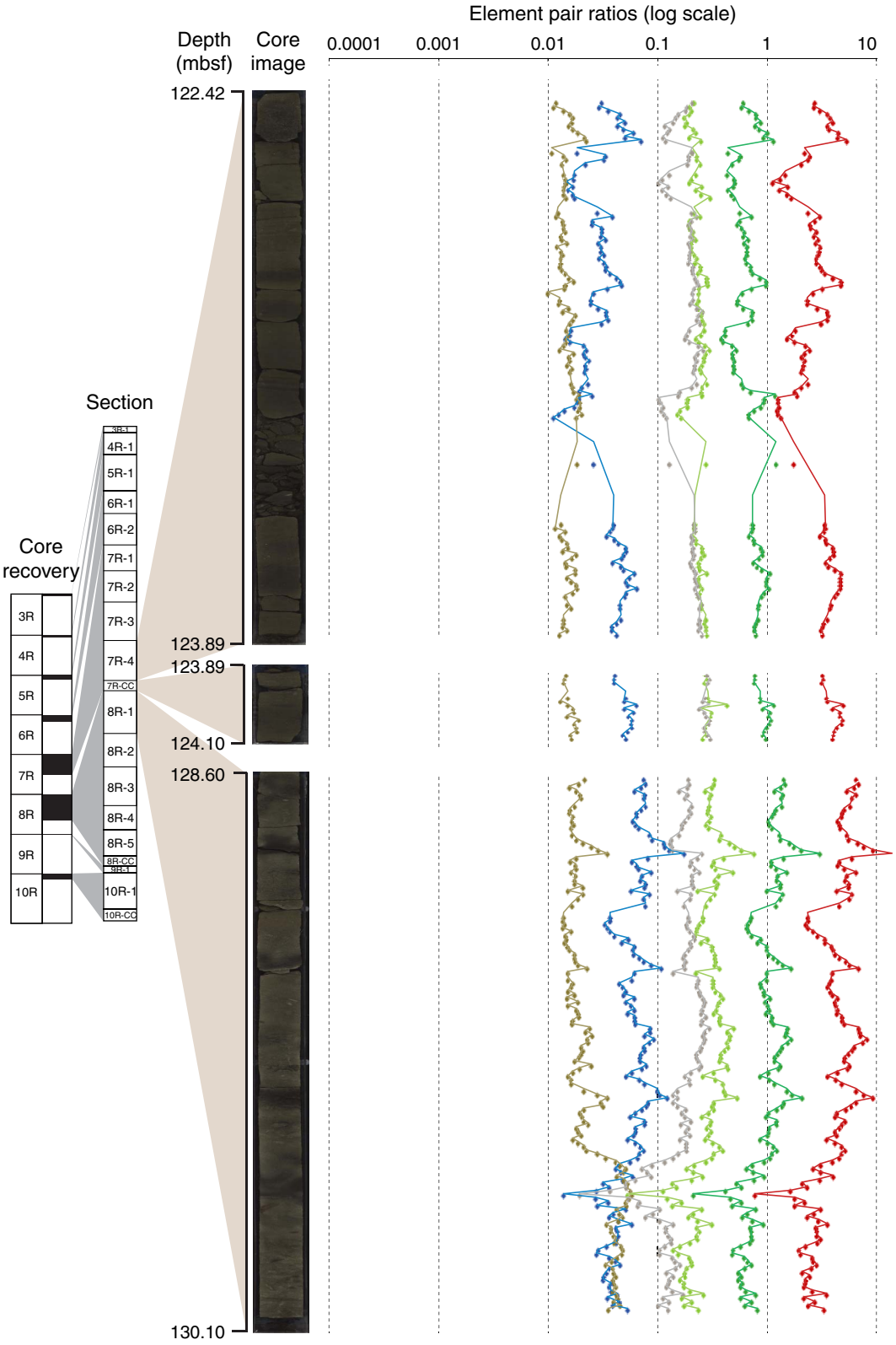

Figure F3 (continued). (Continued on next page.)

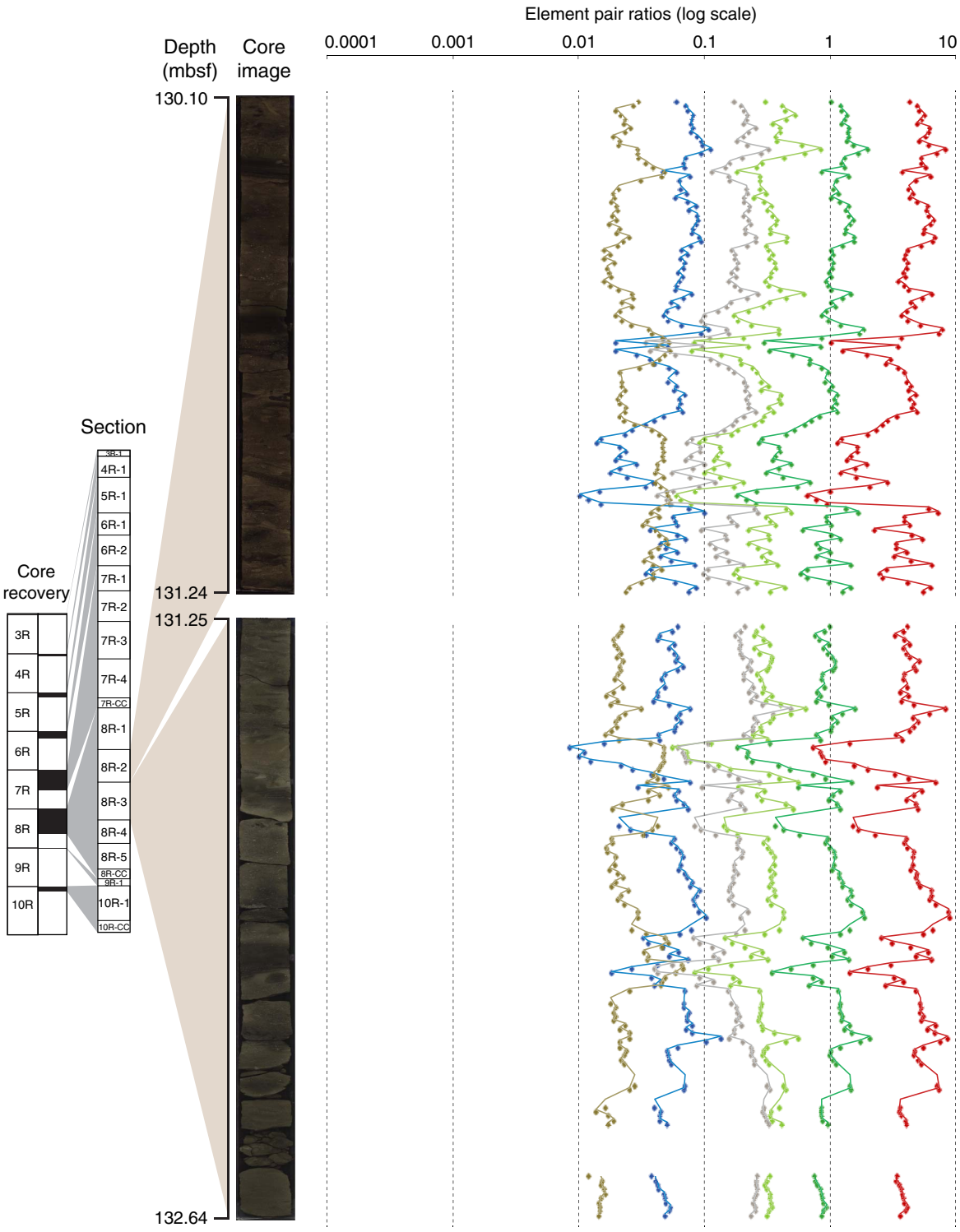

Figure F3 (continued). (Continued on next page.)

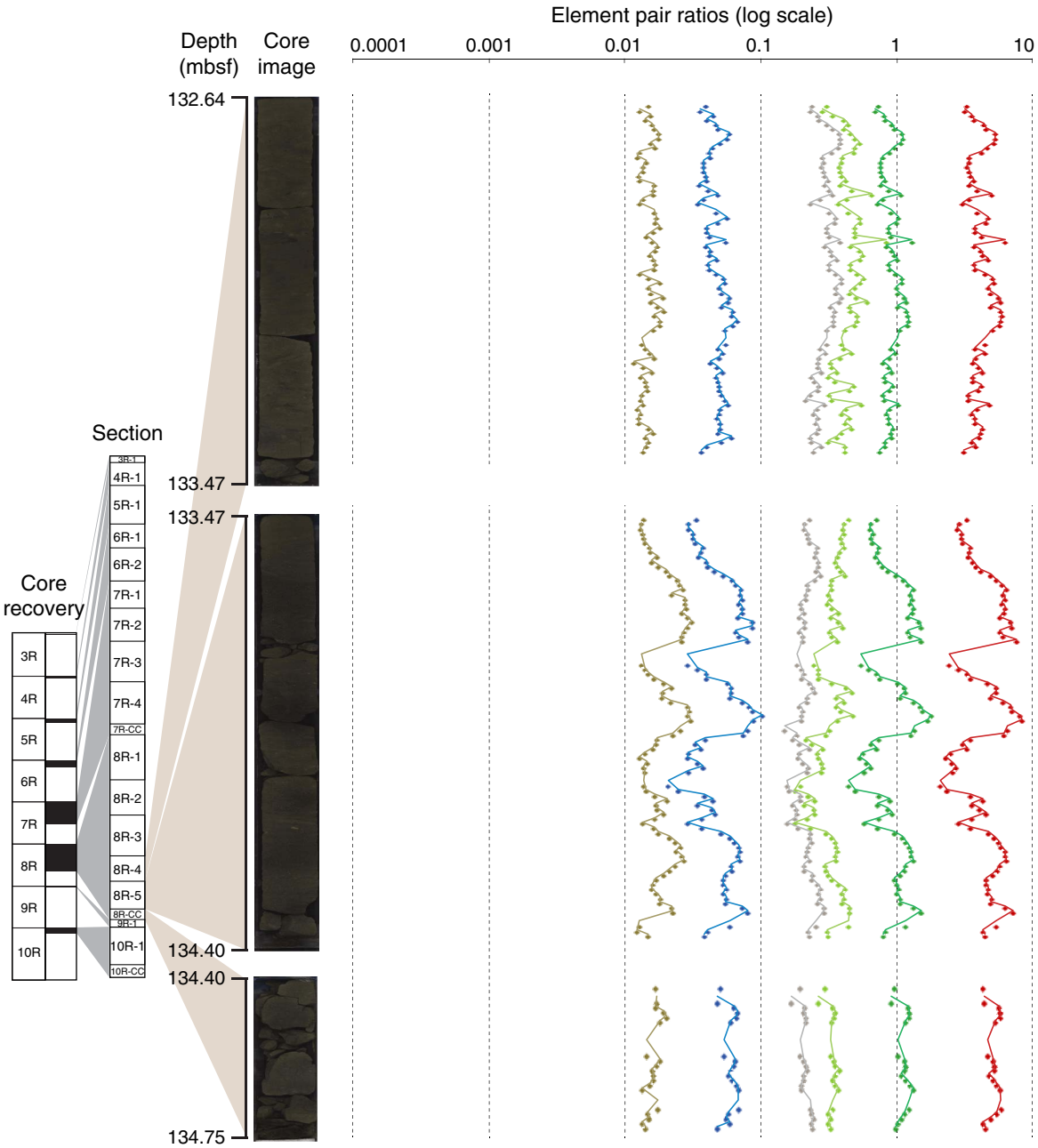

Figure F3 (continued).

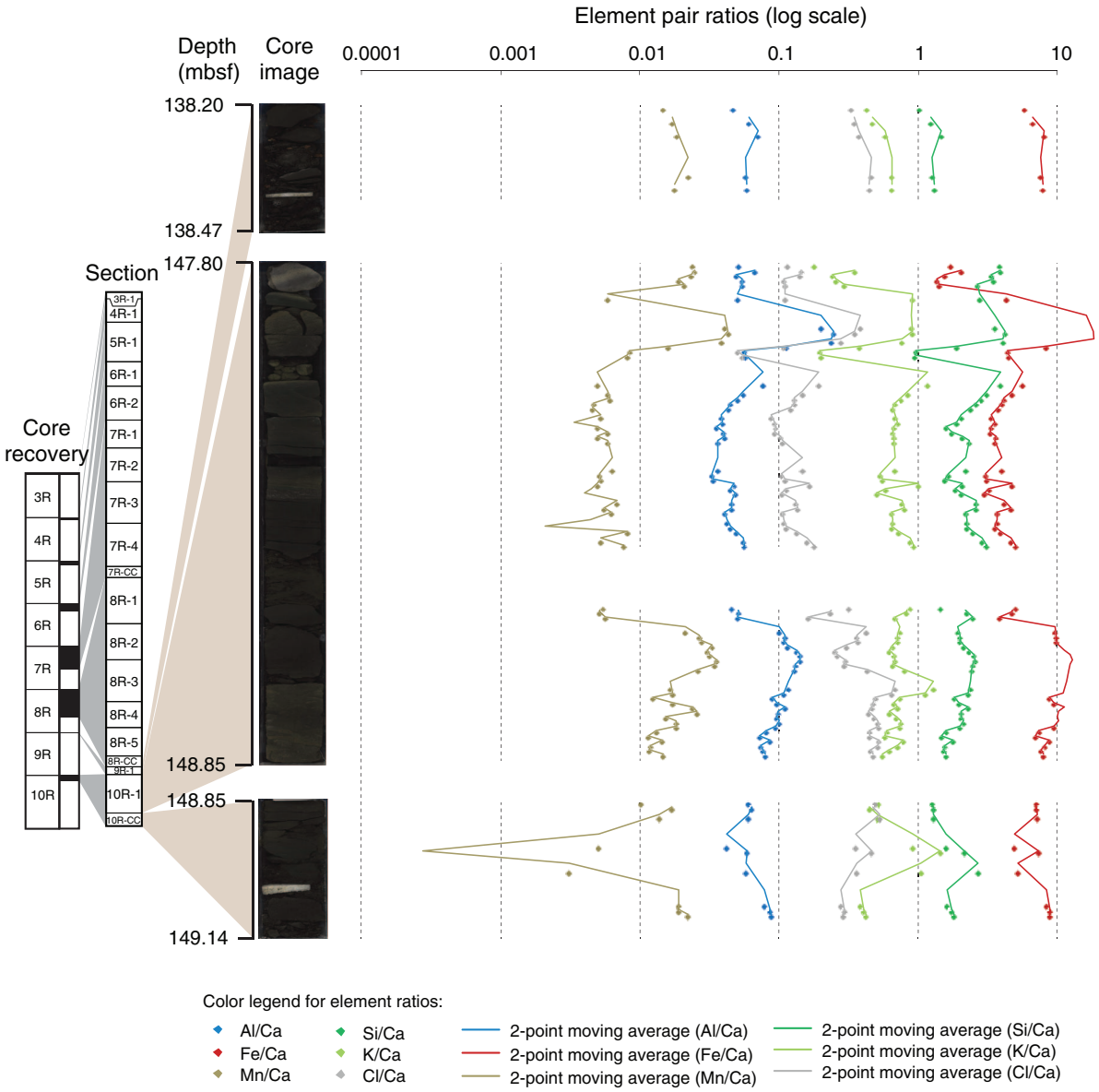

Figure F4. Average of Al/Si (blue), Fe/Si (red), Mn/Si (brown), Ca/Si (dark green), K/Si (light green), and Cl/Si (gray) per section with their variance as error bars. The error bars are visible if the error is larger than the symbol for the data point.

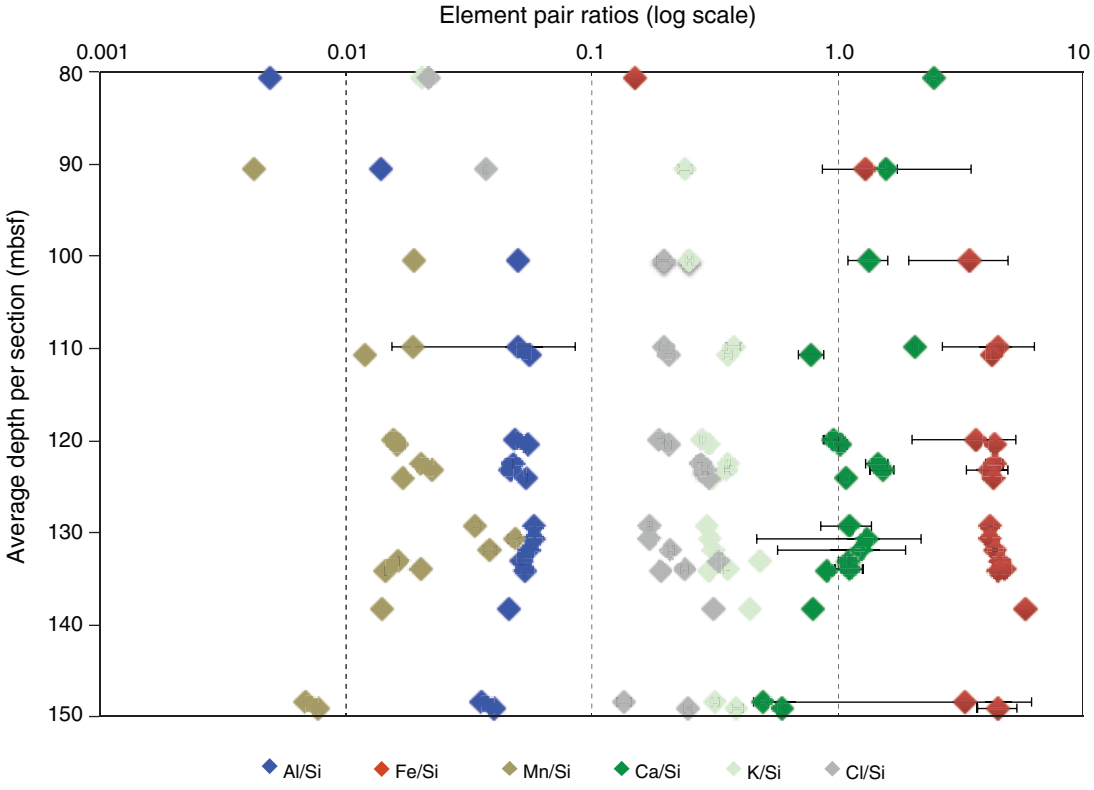

Figure F5. Element pair ratios (Al/Si, Cl/Si, Fe/Si, K/Si, Mn/Si) for all cores vs. Si. Areas of dense point accumulations are (**A**) shaded and (**B**) shown at higher resolution for the same element pair ratios. (Continued on next two pages.)

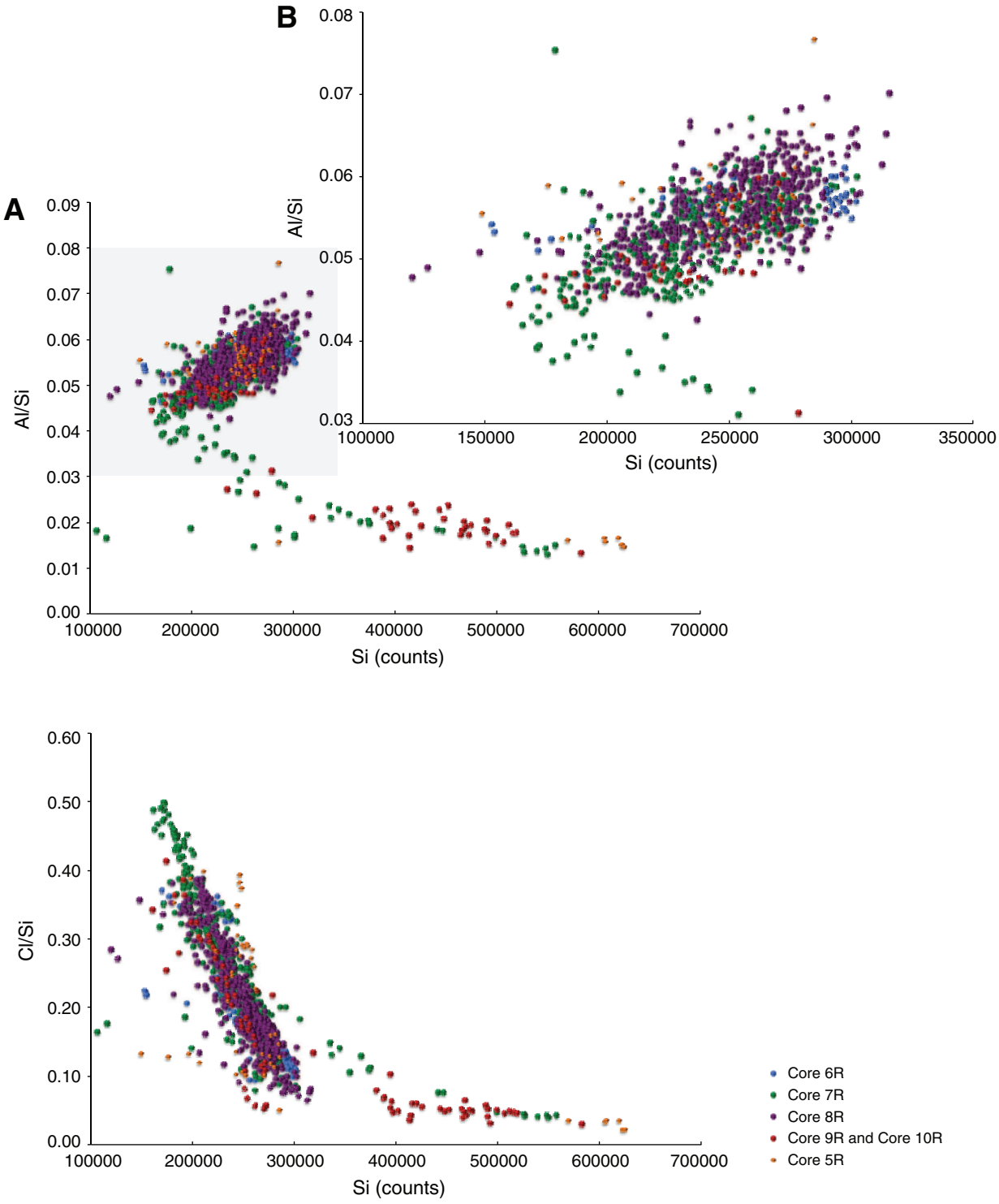

Figure F5 (continued). (Continued on next page.)

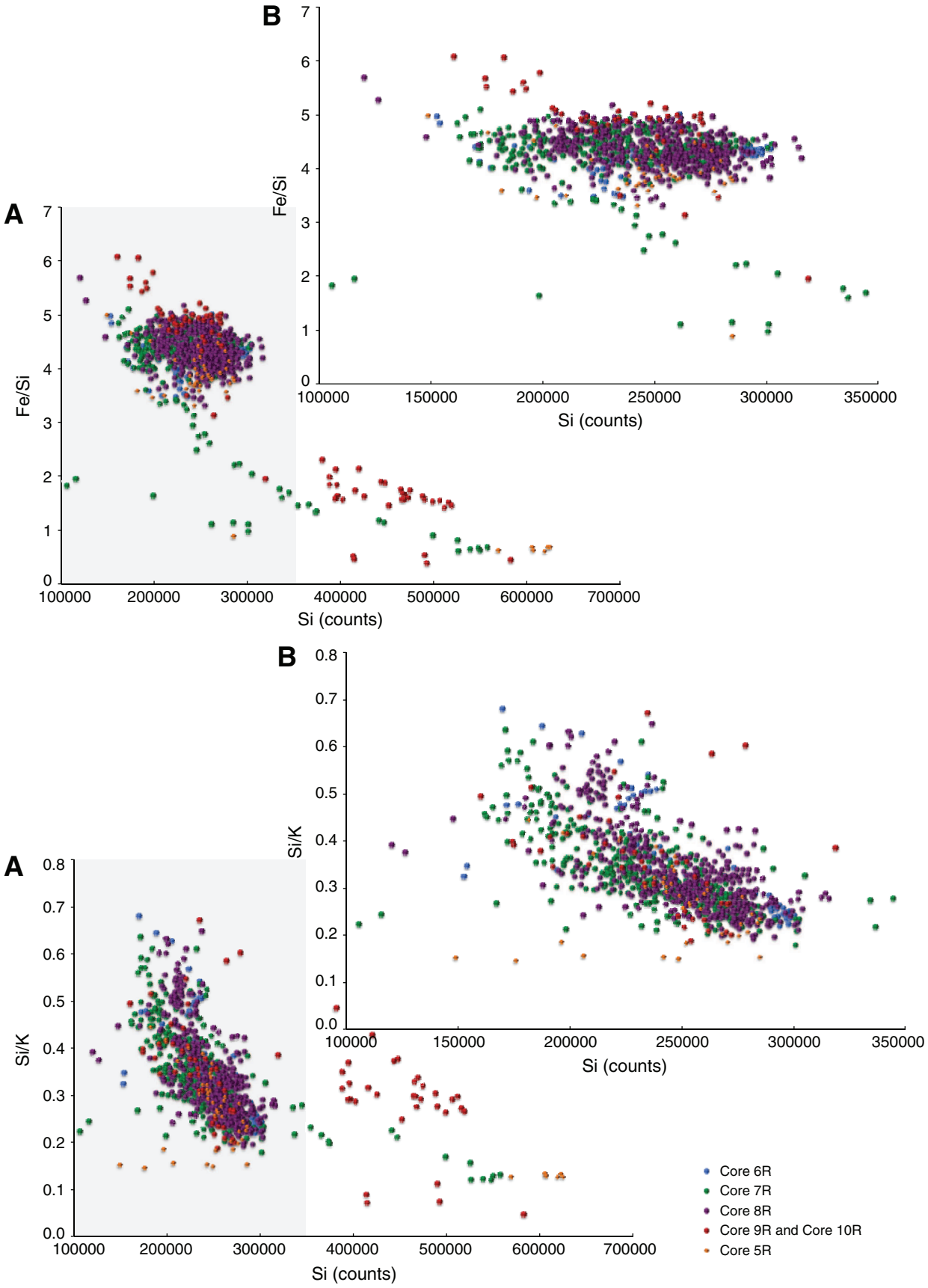

Figure F5 (continued).

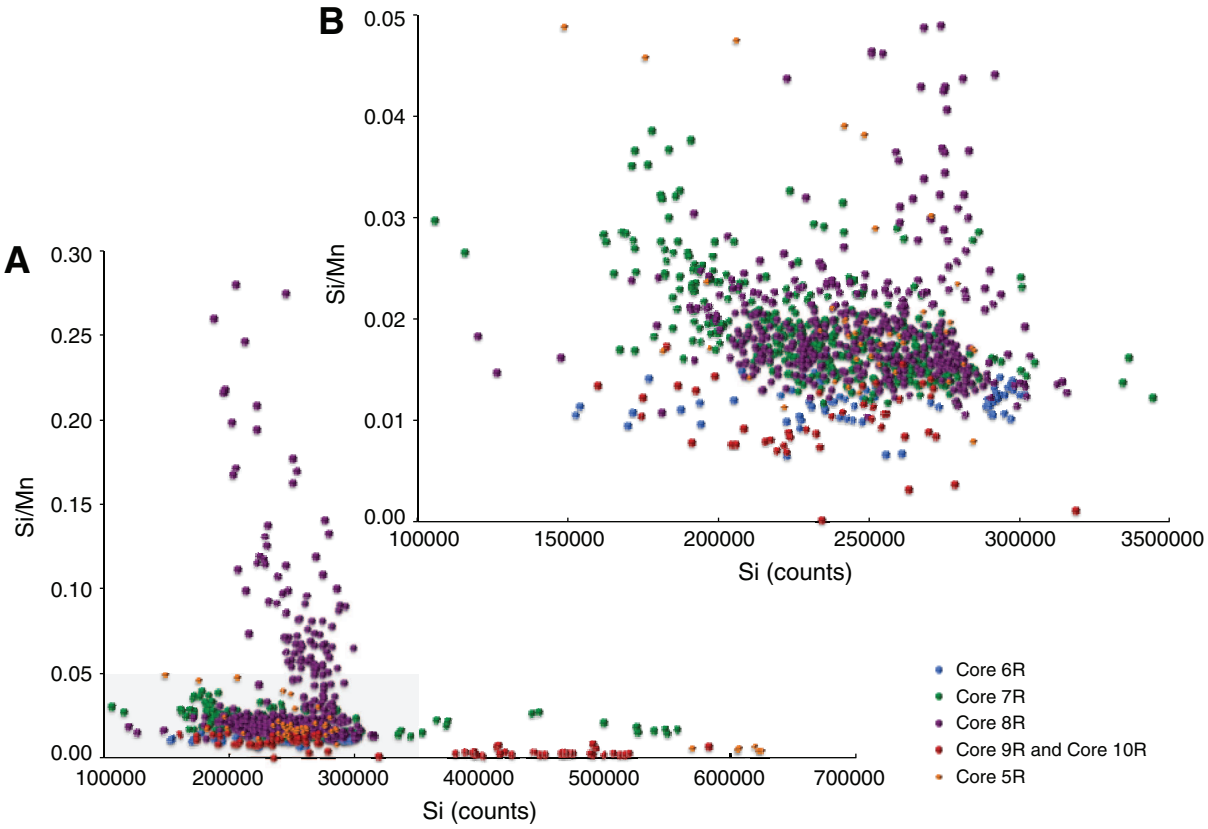

Appendix

Single-element counts for Si, Al, Fe, Mn, Ca, K, and Cl and element pair ratios of those elements with Si and Ca for the analyzed Sections 324-U1347A-3R-1 through 10R-CC are listed in Table **AT1.**

Table AT1. Single element counts and element ratios.

Depth (mbsf)	Single element counts							Element pair ratios												
	Si	Al	Fe	Mn	Ca	K	Cl	Al/Si	Fe/Si	Mn/Si	Ca/Si	K/Si	Cl/Si	Al/Ca	Fe/Ca	Mn/Ca	Si/Ca	K/Ca	Cl/Ca
80.63	593076	2454	59482	592	1480802	6319	10689	0.0041	0.1003	0.0010	2.4968	0.0107	0.0180	0.0017	0.0402	0.0004	0.4005	0.0043	0.0072
80.65	544672	2446	77782	851	1633919	9723	12277	0.0045	0.1428	0.0016	2.9998	0.0179	0.0225	0.0015	0.0476	0.0005	0.3334	0.0060	0.0075
80.66	554658	2769	97229	296	1548211	12768	13366	0.0050	0.1753	0.0005	2.7913	0.0230	0.0241	0.0018	0.0628	0.0002	0.3583	0.0082	0.0086
80.67	611895	3205	84514	471	1238907	13043	14416	0.0052	0.1381	0.0008	2.0247	0.0213	0.0236	0.0026	0.0682	0.0004	0.4939	0.0105	0.0116
80.68	581775	3163	114119	244	1246776	16692	12948	0.0054	0.1962	0.0004	2.1431	0.0287	0.0223	0.0025	0.0915	0.0002	0.4666	0.0134	0.0104
80.69	574438	3082	87236	558	1335497	12338	11853	0.0054	0.1519	0.0010	2.3249	0.0215	0.0206	0.0023	0.0653	0.0004	0.4301	0.0092	0.0089
90.12	1003482	4789	15233	1925	7593	2682	3300	0.0048	0.0152	0.0019	0.0076	0.0027	0.0033	0.6307	2.0062	0.2535	132.1588	0.3532	0.4346
90.17	603292	2116	130778	2259	1644563	16460	6582	0.0035	0.2168	0.0037	2.7260	0.0273	0.0109	0.0013	0.0795	0.0014	0.3668	0.0100	0.0040
90.18	618307	2896	251256	2232	1241885	38283	7026	0.0047	0.4064	0.0036	2.0085	0.0619	0.0114	0.0023	0.2023	0.0018	0.4979	0.0308	0.0057
90.22	477496	9395	1118479	1377	256840	189042	20156	0.0197	2.3424	0.0029	0.5379	0.3959	0.0422	0.0366	4.3548	0.0054	1.8591	0.7360	0.0785
90.23	501513	8781	1117258	859	271317	188546	19402	0.0175	2.2278	0.0017	0.5410	0.3760	0.0387	0.0324	4.1179	0.0032	1.8484	0.6949	0.0715
90.28	516304	9733	1249703	816	209778	201845	18111	0.0189	2.4205	0.0016	0.4063	0.3909	0.0351	0.0464	5.9573	0.0039	2.4612	0.9622	0.0863
90.29	537195	9664	1048688	1231	301482	174486	17282	0.0180	1.9522	0.0023	0.5612	0.3248	0.0322	0.0321	3.4784	0.0041	1.7818	0.5788	0.0573
90.3	511666	10047	1240672	928	192480	204786	17937	0.0196	2.4248	0.0018	0.3762	0.4002	0.0351	0.0522	6.4457	0.0048	2.6583	1.0639	0.0932
90.33	460193	10774	1091341	1086	301207	190392	16724	0.0234	2.3715	0.0024	0.6545	0.4137	0.0363	0.0358	3.6232	0.0036	1.5278	0.6321	0.0555
90.34	543427	10538	966649	1124	294354	166915	16776	0.0194	1.7788	0.0021	0.5417	0.3072	0.0309	0.0358	3.2840	0.0038	1.8462	0.5671	0.0570
90.35	569418	10299	927739	807	291079	160837	17207	0.0181	1.6293	0.0014	0.5112	0.2825	0.0302	0.0354	3.1872	0.0028	1.9562	0.5526	0.0591
90.36	540722	10515	1139243	1184	188294	202574	18961	0.0194	2.1069	0.0022	0.3482	0.3746	0.0351	0.0558	6.0503	0.0063	2.8717	1.0758	0.1007
90.37	470004	9390	888384	1054	193281	167781	19518	0.0200	1.8902	0.0022	0.4112	0.3570	0.0415	0.0486	4.5963	0.0055	2.4317	0.8681	0.1010
90.38	477078	9954	935549	691	161624	181221	18474	0.0209	1.9610	0.0014	0.3388	0.3799	0.0387	0.0616	5.7884	0.0043	2.9518	1.1213	0.1143
90.39	492943	9910	933913	597	177458	179549	17623	0.0201	1.8946	0.0012	0.3600	0.3642	0.0358	0.0558	5.2627	0.0034	2.7778	1.0118	0.0993
90.47	565207	8646	810782	1427	392708	150953	18282	0.0153	1.4345	0.0025	0.6948	0.2671	0.0323	0.0220	2.0646	0.0036	1.4393	0.3844	0.0466
90.48	566963	8370	699218	1870	523677	131814	18347	0.0148	1.2333	0.0033	0.9237	0.2325	0.0324	0.0160	1.3352	0.0036	1.0827	0.2517	0.0350
90.49	569481	8166	656820	1942	567907	125758	17345	0.0143	1.1534	0.0034	0.9972	0.2208	0.0305	0.0144	1.1566	0.0034	1.0028	0.2214	0.0305
90.5	551474	9745	782110	1607	485968	146729	17426	0.0177	1.4182	0.0029	0.8812	0.2661	0.0316	0.0201	1.6094	0.0033	1.1348	0.3019	0.0359
90.51	546351	9375	805301	1434	478990	151212	16135	0.0172	1.4740	0.0026	0.8767	0.2768	0.0295	0.0196	1.6812	0.0030	1.1406	0.3157	0.0337
90.52	484322	9194	716145	942	322361	135270	16552	0.0190	1.4787	0.0019	0.6656	0.2793	0.0342	0.0285	2.2216	0.0029	1.5024	0.4196	0.0513
90.53	429146	9204	756283	665	243484	141808	16909	0.0214	1.7623	0.0015	0.5674	0.3304	0.0394	0.0378	3.1061	0.0027	1.7625	0.5824	0.0694
90.54	368507	7901	678893	1050	284689	127805	16330	0.0214	1.8423	0.0028	0.7725	0.3468	0.0443	0.0278	2.3847	0.0037	1.2944	0.4489	0.0574
90.58	311378	4983	533554	3453	1093236	107649	27011	0.0160	1.7135	0.0111	3.5110	0.3457	0.0867	0.0046	0.4881	0.0032	0.2848	0.0985	0.0247
90.59	302798	5692	615825	3375	1060924	128053	28810	0.0188	2.0338	0.0111	3.5037	0.4229	0.0951	0.0054	0.5805	0.0032	0.2854	0.1207	0.0272
90.6	259811	4997	633206	2983	987765	123249	21958	0.0192	2.4372	0.0115	3.8019	0.4744	0.0845	0.0051	0.6410	0.0030	0.2630	0.1248	0.0222
90.63	235664	3854	400893	6284	1353694	89795	26032	0.0164	1.7011	0.0267	5.7442	0.3810	0.1105	0.0028	0.2961	0.0046	0.1741	0.0663	0.0192
90.76	658228	4137	247482	2203	1035191	38435	12449	0.0063	0.3760	0.0033	1.5727	0.0584	0.0189	0.0040	0.2391	0.0021	0.6359	0.0371	0.0120
90.79	385657	3776	491967	8610	1525037	103064	19095	0.0098	1.2757	0.0223	3.9544	0.2672	0.0495	0.0025	0.3226	0.0056	0.2529	0.0676	0.0125
90.8	459076	4201	365361	3785	1011258	71980	20975	0.0092	0.7959	0.0082	2.2028	0.1568	0.0457	0.0042	0.3613	0.0037	0.4540	0.0712	0.0207
90.81	431504	3087	357768	3406	889489	60152	20553	0.0072	0.8291	0.0079	2.0614	0.1394	0.0476	0.0035	0.4022	0.0038	0.4851	0.0676	0.0231
99.82	621454	9411	422207	2556	244044	81812	14106	0.0151	0.6794	0.0041	0.3927	0.1316	0.0227	0.0386	1.7300	0.0105	2.5465	0.3352	0.0578
99.83	623881	9227	421001	2692	235214	79305	13496	0.0148	0.6748	0.0043	0.3770	0.1271	0.0216	0.0392	1.7899	0.0114	2.6524	0.3372	0.0574
99.93	246617	12943	1090667	3151	249332	82873	67701	0.0525	4.4225	0.0128	1.0110	0.3360	0.2745	0.0519	4.3744	0.0126	0.9891	0.3324	0.2715
99.98	251722	14411	968013	7276	300557	46290	25361	0.0572	3.8456	0.0289	1.1940	0.1839	0.1008	0.0479	3.2207	0.0242	0.8375	0.1540	0.0844
99.99	270353	15587	1061307	8132	294727	49901	27178	0.0577	3.9256	0.0301	1.0902	0.1846	0.1005	0.0529	3.6010	0.0276	0.9173	0.1693	0.0922
100	279511	15102	1156379	6542	289025	57581	31906	0.0540	4.1372	0.0234	1.0340	0.2060	0.1141	0.0523	4.0010	0.0226	0.9671	0.1992	0.1104
100.02	205635	12180	986540	9765	383371	32123	24644	0.0592	4.7975	0.0475	1.8643	0.1562	0.1198	0.0318	2.5733	0.0255	0.5364	0.0838	0.0643
100.04	175538	10349	818400	8034	338777	25689	22595	0.0590	4.6622	0.0458	1.9299	0.1463	0.1287	0.0305	2.4157	0.0237	0.5182	0.0758	0.0667
100.05	148601	8243	742754	7245	299881	22509	19615	0.0555	4.9983	0.0488	2.0180	0.1515	0.1320	0.0275	2.4768	0.0242	0.4955	0.0751	0.0654
100.09	241828	14228	1007007	9458	406414	37389	24715	0.0588	4.1641	0.0391	1.6806	0.1546	0.1022	0.0350	2.4778	0.0233	0.5950	0.0920	0.0608
100.1	248148	14211	1047920	9469	435680	37172	26422	0.0573	4.2230	0.0382	1.7557	0.1498	0.1065	0.0326	2.4053	0.0217	0.5696	0.0853	0.0606

Only a portion of this table appears here. The complete table is available in **ASCII.**